Eur. Phys. J. D **31**, 11–19 (2004)
DOI: 10.1140/epjd/e2004-00125-0

THE EUROPEAN PHYSICAL JOURNAL D

Kinetic energy distributions in pionic hydrogen

T.S. Jensen[a]

Laboratoire Kastler–Brossel, École Normale Supérieure et Université Pierre et Marie Curie, Case 74, 4 place Jussieu, 75252 Paris Cedex 05, France

Received 17 June 2004 / Received in final form 6 August 2004
Published online 28 September 2004 –

Abstract. A framework for analyzing the Doppler broadening of the X–ray lines in pionic hydrogen is proposed. It is shown that the kinetic energy distributions at the instant of the $np \rightarrow 1s$ ($n = 2$–4) radiative transitions are related to each other. In order to establish the connection, the collisional processes for pionic hydrogen scattering from hydrogen atoms and molecules have been calculated in different models. The proposed method can be used to determine reliably the strong interaction width of the ground state of pionic hydrogen from the X–ray line profiles measured recently at the Paul–Scherrer–Institut.

PACS. 34.50.-s Scattering of atoms and molecules – 36.10.Gv Mesonic atoms and molecules, hyperonic atoms and molecules

1 Introduction

Pionic hydrogen atoms ($\pi^- p$) are formed when negative pions stop in hydrogen. After the formation in highly excited states, the $\pi^- p$ atoms deexcite to lower lying levels through a number of processes (external Auger effect, radiative transitions, and Coulomb deexcitation) until nuclear capture or weak decay take place. A good understanding of the life history, the so–called atomic cascade, of pionic hydrogen and other exotic atoms is important for the planning and interpretation of several experiments (see Ref. [1] for a review).

In the present paper we will deal with the problem of extracting the $1s$ strong interaction width, $\Gamma_{1s}^{\rm had}$, of pionic hydrogen from measured X–ray line profiles. The finite width of the $1s$ state is due to $\pi^- p$ decay to $\pi^0 + n$ and $\gamma + n$. Strong interaction also changes the energy of the $1s$ state shifting it below the QED value. Using Deser type formulas [2], the strong interaction width and shift are related to the pion–nucleon scattering lengths which are of great importance in hadronic physics. A detailed investigation of the strong energy shift and the pion–nucleon s–wave scattering lengths is given in reference [3]. The width was determined at the Paul–Scherrer–Institut (PSI) and is given by [4]

$$\Gamma_{1s}^{\rm had} = 0.868 \pm 0.040({\rm stat.}) \pm 0.038({\rm syst.})\ {\rm eV}. \qquad (1)$$

The new pionic hydrogen $1s$ shift/width experiment at PSI [5] aims at determining $\Gamma_{1s}^{\rm had}$ with a precision better than 2%. The profiles of the $np \rightarrow 1s$ X–ray lines in $\pi^- p$ are largely given by a convolution of a Lorentzian with width $\Gamma_{1s}^{\rm had}$ and a Doppler broadening profile due to the non–thermal motion of the $\pi^- p$ atoms in the target. In order to extract the strong interaction width from measured X–ray spectra, procedures for subtracting the Doppler broadening must be applied. The observed line width for a given transition is related to the $1s$ strong interaction width: $\Gamma^{\rm obs.} = (1 + \Delta_D)\Gamma_{1s}^{\rm had}$. In the previous experiment [4], measuring the $3p \rightarrow 1s$ transition, the Doppler broadening correction to the width was estimated to be $\Delta_D = 12 \pm 5\%$. The uncertainty is responsible for the systematic error in equation (1). The kinetic motion of the $\pi^- p$ atoms at the moment of the radiative transitions depends on the atomic cascade and can be predicted by ab initio cascade model calculations. Those calculations are, however, difficult as they require a detailed understanding of the acceleration and deceleration mechanisms. Here an alternative strategy, which depends on more reliable cascade model input, will be explored. The proposed method combines a fitting procedure for the line profiles with constraints that are based on cross–sections at high energies (>10 eV) which can be calculated more accurately than those at low energies.

The outline of this paper is as follows: Section 2 discusses the atomic cascade in pionic hydrogen. A cascade model dealing only with the evolution of the high energy components in pionic hydrogen is presented in Section 3. In Section 4, a framework for analyzing the kinetic energy distributions which evolve at low n is presented. The scattering of $\pi^- p$ from atomic and molecular hydrogen is studied in Section 5. Section 6 presents the results and Section 7 summarizes the conclusions.

[a] e-mail: Thomas.Jensen@spectro.jussieu.fr

2 Atomic cascade

Atomic cascade was studied theoretically more than forty years ago by Leon and Bethe [6]. In their framework, and later in more refined models [7,8], the rates for the collisional processes were calculated at a fixed kinetic energy (typically 1 eV) and used to simulate the atomic cascade. The success of these models derives from the fact they give a good description of the X–ray yields.

The PSI shift/width experiment [5], however, requires a more sophisticated approach because it depends on knowing the kinetic energy distribution at some instant during the cascade. Beginning with Markushin [9] recent cascade models take into account the acceleration and deceleration of the exotic atoms produced in collisions with the target atoms. The extended standard cascade model (ESCM) which was presented in references [10–13] introduces a number of improvements compared to the earlier models: for example, the scattering from *molecular* hydrogen at high n is calculated in detail [11] as opposed to the phenomenological treatment in other cascade studies. Our present understanding of the life history of $\pi^- p$ atoms can be summarized as follows:

- the $\pi^- p$ atoms are formed by atomic capture by target protons resulting in a broad distribution in the principal quantum number around $n = 15$, see reference [14] and references therein. The initial kinetic energy is expected to be similar to that of muonic hydrogen. An analysis of muonic hydrogen diffusion data suggests that a median kinetic energy of 0.5 eV after formation is realistic [12];
- the deexcitation at $n > 8$ takes place mainly through the process [11]

$$(\pi^- p)_n + \mathrm{H}_2 \rightarrow \begin{cases} (\pi^- p)_{n'} + \mathrm{H}_2^* \\ (\pi^- p)_{n'} + \mathrm{H} + \mathrm{H} \end{cases} \quad n' < n \,. \quad (2)$$

  Most $\pi^- p$ atoms will accelerate to energies of a few electron volts during this stage;
- in the intermediate part of the cascade, $n = 7{-}8$, the Auger transitions

$$(\pi^- p)_n + \mathrm{H} \rightarrow (\pi^- p)_{n'} + p + e^-, \quad n' < n \quad (3)$$

  dominate;
- at $n = 2 - 6$ there are several competing processes: radiative, Auger, and Coulomb transitions, and nuclear absorption. This makes reliable cascade calculations difficult as the collisional rates have to be calculated fairly accurately. Some observables like cascade times and relative X–ray yields are, however, less sensitive to uncertainties in the cross–sections.

The highly energetic $\pi^- p$ atoms are created via the Coulomb deexcitation process [15,16]

$$(\pi^- p)_n + \mathrm{H} \rightarrow (\pi^- p)_{n'} + \mathrm{H}, \quad n' < n. \quad (4)$$

The energy released in an $n \rightarrow n'$ Coulomb transition is given by (we use atomic units: $e = m_e = \hbar = 1$)

$$\Delta E_{n \rightarrow n'} = \frac{M_{\mathrm{red}}}{2} \left(\frac{1}{n'^2} - \frac{1}{n^2} \right) \quad (5)$$

where M_{red} is the reduced mass of the $\pi^- p$ atom. At low n only $\Delta n = 1$ transitions are expected to be important so the highly energetic $\pi^- p$ atoms will have the characteristic kinetic energies

$$T_n = \frac{M_{\mathrm{H}}}{M_{\mathrm{H}} + M_{\pi^- p}} \Delta E_{n+1 \rightarrow n} \quad (6)$$

where M_{H} and $M_{\pi^- p}$ are the masses of the hydrogen atom and the $\pi^- p$ atom, respectively. Equation (6) gives the energies 18 eV, 34 eV, 73 eV, and 209 eV for $n = 5$, 4, 3, and 2.

Coulomb deexcitation can also take place via the formation of the molecular states [17]:

$$(\pi^- p)_n + \mathrm{H}_2 \rightarrow \left(\{\pi^- pp\}^* pee \right)^* \quad (7)$$

where the three–body system $\{\pi^- pp\}^*$ lies below the $(\pi^- p)_n + p$ dissociation limit. The complex, $(\{\pi^- pp\}^* pee)^*$, can decay through a number of channels: Coulomb, Auger, and radiative deexcitation, nuclear absorption, and back decay.

Both the direct Coulomb deexcitation process (4) and the formation of molecular states (7) are expected to dominate at low energies but the present quantitative understanding of them is not adequate for an ab initio calculation of the kinetic energy distributions to the precision required by the pionic hydrogen shift/width experiment.

The existence of high energy components has been established in pionic hydrogen in the neutron time–of–flight experiment [18] and in muonic hydrogen in diffusion experiments [19,20]. In the last case, the collisional quenching of the metastable $2s$ state resulted in highly energetic (0.9 keV) $(\mu p)_{1s}$ atoms which were observed in the time–of–flight spectrum. The $2s \rightarrow 1s$ quenching rate was found to be 4×10^{11} s^{-1} when normalized to liquid density [19]. We will show in Section 6.1 that an analysis of the $np \rightarrow 1s$ X-ray spectra in pionic hydrogen makes it possible to estimate Coulomb deexcitation rates here, too.

3 Cascade model for the high energy components

In 2002 the X–ray spectra of the $4p \rightarrow 1s$, $3p \rightarrow 1s$, and $2p \rightarrow 1s$ transitions were measured with good statistics at PSI at a density corresponding to 10 bar. The Doppler broadening corrections to the line widths differ in the three cases because the $\pi^- p$ kinetic energy distributions are not similar at the different n levels: for example, the $3 \rightarrow 2$ Coulomb transitions give rise to a 209 eV component which only contributes to the broadening of the $2p \rightarrow 1s$ line. The Doppler broadening corrections in the three spectra are, however, not independent. The $\pi^- p$ atoms that go through the $4 \rightarrow 3$ Coulomb transition gaining 73 eV in kinetic energy contribute to both the $3p \rightarrow 1s$ and $2p \rightarrow 1s$ line broadening because they can go through the $3d \rightarrow 2p$ radiative transition without losing kinetic energy. Likewise, the $5 \rightarrow 4$ Coulomb component is expected to

contribute to all three measured spectra. This observation is used in the framework described in Section 4.

The proposed method for analyzing the X–ray spectra treats the low energy population of $\pi^- p$ atoms as a "black box" whereas cascade calculations are done for the high energy fraction. We consider the kinetic energy as being low when molecular target effects are very important and the collisional processes are difficult to calculate. In the following we use 10 eV as the kinetic energy separating the low and high energy components.

An atomic cascade simulation program that only deals with the high energy/low n part of the cascade has been written. The program follows the life history of a large ensemble of $\pi^- p$ atoms starting from an initial distribution in the quantum numbers n and l and kinetic energy. The population of the quantum numbers n and l and the kinetic energy are modified by both collisional and non–collisional processes. The non–collisional processes included are radiative deexcitation and nuclear absorption from the ns states. The most important collisional processes are

$$(\pi^- p)_{nl_1} + \mathrm{H} \rightarrow \begin{cases} (\pi^- p)_{nl_2} + \mathrm{H} & \text{(Stark/elastic)} \\ \pi^0(\gamma) + n + \mathrm{H} & \text{(Absorption)} \end{cases} . \quad (8)$$

These processes are calculated as described in Section 5. The external Auger effect

$$(\pi^- p)_n + \mathrm{H} \rightarrow (\pi^- p)_{n-1} + p + e^- \quad (9)$$

is also included though it is dominated by absorption at low n. The Auger deexcitation rates have been calculated in the Born approximation [6] which is in good agreement with the more accurate eikonal approximation for the range of quantum number n and kinetic energies considered here [11]. Coulomb deexcitation is expected only to take place from the low energy component and is, therefore, not included in the model.

The $\pi^- p$ atoms lose kinetic energy in the collisions (8). This is taken into account in the cascade model which uses the differential cross–sections

$$\frac{\mathrm{d}\sigma_n^{\mathrm{av}}}{\mathrm{d}\theta} \quad (10)$$

to calculate the kinetic energy loss in each collision. σ_n^{av} denotes the l-averaged cross-section with $l > 0$

$$\sigma_n^{\mathrm{av}} = \frac{1}{n^2 - 1} \sum_{l_1=1}^{n-1} (2l_1 + 1) \sum_{l_2=1}^{n-1} \sigma_{nl_1 \rightarrow nl_2}. \quad (11)$$

In the case of molecular target the same program is used with all collisional rates multiplied by the energy dependent ratios $\sigma_n^{\mathrm{mol}}/2\sigma_n^{\mathrm{atom}}$ where σ_n^{mol} and σ_n^{atom} are the total l–averaged Stark cross–sections for scattering on hydrogen molecules and atoms, respectively.

With the cascade program it is possible to calculate the X–ray signal from a given high energy component. For example, the fractions of the $5 \rightarrow 4$ Coulomb component that go through the $np \rightarrow 1s$ radiative transitions for $n = 2{-}4$ as well as the kinetic energy distributions at the instant of the radiative transition are calculated. Though the initial population at $n = 4$ with energy 34 eV is not known, the calculation of the X–ray signal it produces can be used in a combined analysis of the spectra as discussed in Section 4.

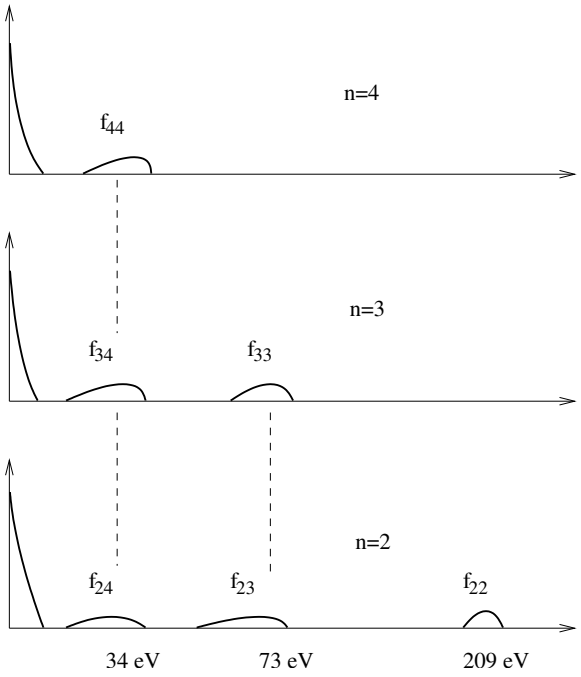

Fig. 1. Schematic view of the kinetic energy distributions at the instant of the $np \rightarrow 1s$ radiative transitions in $\pi^- p$ for $n = 2{-}4$. The discrete energy components have the weights f_{mn} which can be determined by cascade calculations, a fitting procedure, or a combination of both.

4 Constraints on the high energy components

In order to extract the $1s$ strong interaction width from the X–ray spectra the kinetic energy distribution at the instant of the radiative transition is needed. As illustrated in Figure 1, one can divide the distribution into different components

$$0 \leq f_{mn} \leq 1 \quad (12)$$

where the subscript indicates the level (m) from which the radiative transition takes place and the level (n) where the Coulomb component first appears. For example, f_{24} is the 34 eV component in the K_α spectrum. The rest can be collected into low energy components

$$f_n^{\mathrm{low}} = 1 - f_{nn+1} - f_{nn+2} - ... \quad (13)$$

which contain those surviving atoms that arrive at the level n with low energies and those which slow down from higher energies.

A $np \rightarrow 1s$ X–ray line profile is given by a convolution of a Lorentzian with the width $\Gamma_{1s}^{\mathrm{had}}$ and a Doppler profile derived from the kinetic energy distribution. With no

more knowledge of the atomic cascade than the existence of the Coulomb components, the determination of $\Gamma_{1s}^{\rm had}$ from the measured line profiles could be carried out by applying a fitting procedure in which the weights, f_{mn}, are free parameters (in addition to $\Gamma_{1s}^{\rm had}$). The problem with this method is that the $\pi^- p$ atoms may have experienced kinetic energy loss in collisions before they deexcite radiatively. The high energy components will, therefore, in general be broad distributions with the maximal kinetic energy extending up to the characteristic energy given by equation (6).

Because of this problem, we suggest improving the method by using the results of the atomic cascade program presented here. The calculated kinetic energy distributions should then substitute the single energy components in the fitting procedure. Another benefit from using the cascade program is that one can obtain the ratios $f_{m_1 n}/f_{m_2 n}$ as we will show now.

The cascade program does not allow us to calculate f_{mn} because the $n+1 \to n$ Coulomb yield is to be treated as an unknown. What can be calculated is the fraction of the $\pi^- p$ atoms in the $n+1 \to n$ Coulomb component at the level n, which go through the $mp \to 1s$ radiative transition while still having high kinetic energies. It is given by

$$g_{mn} = \frac{Y_m^{\rm rad}}{Y_n^{\rm Coul}} f_{mn}, \quad m \le n \tag{14}$$

where $Y_n^{\rm Coul}$ denotes the $n+1 \to n$ Coulomb yield and $Y_m^{\rm rad}$ the $mp \to 1s$ radiative yield. At first the relation (14) does not seem to help us much as it contains the unknown $Y_n^{\rm Coul}$ and the radiative yield $Y_m^{\rm rad}$ which has been measured with a statistical uncertainty of 20–30% for K_γ and 10–20% for K_α and K_β [21]. The situation improves when one considers the ratio

$$\frac{g_{m_1 n}}{g_{m_2 n}} = \frac{Y_{m_1}^{\rm rad}}{Y_{m_2}^{\rm rad}} \frac{f_{m_1 n}}{f_{m_2 n}} \tag{15}$$

where the dependence on $Y_n^{\rm Coul}$ has disappeared and one only needs to know the X–ray intensity ratios which are experimentally easier to determine. The ratios $f_{m_1 n}/f_{m_2 n}$ can then be used in the fitting procedure reducing the number of unknown parameters significantly: for example, the six free weights in the three kinetic energy distributions in Figure 1 are reduced to three. The constraints will make a more precise determination of $\Gamma_{1s}^{\rm had}$ possible as compared to what can be obtained from three independent analyses of the spectra.

5 Scattering of pionic hydrogen from hydrogen

The framework described in Section 4 requires good quantitative understanding of the cascade processes at kinetic energies higher than 10 eV and principal quantum numbers $n = 2{-}4$. We will show in Section 5.1 that the semiclassical straight–line–trajectory approximation of Kodosky and Leon [22], in which the $\pi^- p$ atom is treated quantum mechanically and assumed to move along a straight line with constant velocity through the electric field of the target, is a good approximation to more accurate models. Furthermore, it also applies to the more realistic case of collisions with H_2 molecules. It was used by Cohen and Struensee [23] to study the problem of muonic helium in the $2s$ state scattering from D_2 at very high energies. The cross–sections for molecular target are calculated in Section 5.2 and compared to the atomic ones.

5.1 Scattering from hydrogen atoms

In the following, $\mathbf{R}$ denotes the vector from the target hydrogen atom to the centre–of–mass of the $\pi^- p$ atom. The vector from the proton in $\pi^- p$ atom to the pion is denoted by $\mathbf{r}$.

Four different models for calculating the cross–sections of $\pi^- p$ scattering from hydrogen atoms have been studied:

- the fully quantum mechanical close coupling (CC) model described in reference [10];
- the semiclassical (SC) model of reference [10]. The radial distance $R = |\mathbf{R}|$ is treated as a classical variable;
- the straight–line–trajectory (SLT) approximation of Kodosky and Leon [22]. The inter–atomic vector $\mathbf{R}$ is a classical variable;
- the fixed field (FF) approximation.

In reference [10] a close coupling model was used to calculate cross–sections for the Stark and absorption processes (8). In this model $\pi^- p$ wave function is expanded into the set of n^2 Coulomb eigenstates with the same quantum number n. The S–matrix is obtained after solving the radial Schrödinger equation for each partial wave. As shown in reference [10], a partial decoupling of the n^2 coupled second order differential equations is possible because of parity conservation.

In the kinetic energy range considered here (>10 eV) many partial waves contribute to the cross–sections (8) and the energy splitting within each atomic level is small compared to the collision energy. Under these circumstances the SC model of reference [10] is a good approximation. In this model the radial distance $R = R(t)$ is a classical variable while the rest of the system consisting of five variables (θ, ϕ, and $\mathbf{r}$) is described quantum mechanically. The time dependent Schrödinger equation has the same symmetries as in the CC model but the coupled equations are of first order making numerical solutions easier to obtain. A similar model has been used by Sakamoto (see [24] and references therein) to study other scattering problems.

One can go one step further and also treat the angular coordinates, θ and ϕ, classically. The collisional processes are calculated by considering classical trajectories, $\mathbf{R}(t)$, through the electric field, $\mathbf{E}(\mathbf{R})$, of the target atoms. The electric field from a hydrogen atom is given by $\mathbf{E}(\mathbf{R}) = F(R)\mathbf{R}/R$ where (with electron screening taken

into account)

$$F(R) = \frac{1}{R^2}(1 + 2R + 2R^2)\exp(-2R). \quad (16)$$

As both projectile and target are neutral in the present case, we let the $\pi^- p$ atoms move with constant velocity, v, along a straight line. This corresponds to the model of Kodosky and Leon [22]. Reifenröther and Klempt [25] studied the scattering of pionic hydrogen on hydrogen atoms using a classical–trajectory model. For the present problem with the fairly high collision energy, the simplifying assumption of uniform movement is, as we will show below, adequate. The time dependent Schrödinger equation is written in matrix form:

$$i\frac{\mathrm{d}A}{\mathrm{d}t} = (V(\mathbf{R}(t)) + \Delta E)A(t) \quad (17)$$

with the initial condition $A(-\infty) = I$. The columns in $A(t)$ contain the time dependent coefficients for the expansion of the wave function into the n^2 Coulomb states $|nlm\rangle$. The potential, $V(\mathbf{R})$, which is responsible for the Stark transitions, is an $n^2 \times n^2$ matrix with elements

$$\langle f|\mathbf{r}\cdot\mathbf{E}(\mathbf{R})|i\rangle = \langle f|x|i\rangle E_x + \langle f|y|i\rangle E_y + \langle f|z|i\rangle E_z \ , \quad (18)$$

where $|i\rangle$ and $|f\rangle$ represent initial and final states in the basis $|nlm\rangle$. The energy shifts and widths are contained in the diagonal matrix ΔE. The set of coupled differential equations (17) is solved for 2000 values of the impact parameter, b, in the interval $0{-}4a_0$. The probability for the transition $i \to f$ $(i \neq f)$ for the impact parameter b is given by

$$P_{i\to f}(b) = |\langle f|A(\mathbf{R}(\infty))|i\rangle|^2. \quad (19)$$

The cross–section is obtained by integration over b:

$$\sigma_{i\to f} = 2\pi \int_0^\infty bP_{i\to f}(b)\mathrm{d}b. \quad (20)$$

The cascade model of Section 3 does not calculate the population over the magnetic quantum number but uses only the cross–sections

$$\sigma_{nl\to nl'} = \frac{1}{2l+1}\sum_{m,m'}\sigma_{nlm\to nl'm'}. \quad (21)$$

The fixed field approximation corresponds to the substitution

$$\langle f|\mathbf{r}\cdot\mathbf{E}|i\rangle \to \langle f|z|i\rangle|\mathbf{E}| \quad (22)$$

i.e. the electric field is assumed to be directed along the z–axis all through the collision. This approximation has been popular in the study of Stark transitions in exotic hydrogen [6,8] because of the simplifications gained in cases where the level with quantum number n can be considered to be degenerate. This is nearly so in the case studied here because the collision energies are much larger than the ns shifts and widths (the largest being the $2p - 2s$ energy difference of 1.25 eV[1]). The differential equations decouple completely after a basis transformation from the Coulomb states $|nlm\rangle$ to the Stark states $|nn_1m\rangle$, see references [6,8], and one is left with a set of first order differential equations which can be integrated directly.

Table 1. The cross–sections in units of a_0^2 for $\pi^- p$ scattering from hydrogen atoms at the laboratory kinetic energy 73 eV calculated in the CC model, the SC model, the SLT approximation, and the FF approximation. The results of the SC model with the $3s$ shift and width set to zero (SC0) are shown as well. In the SLT and the FF approximation the $3s$ shift and width were also set to zero.

	CC	SC	SC0	SLT	FF
$3p \to 3s$+abs.	0.674	0.671	0.688	0.688	0.771
$3p \to 3p$	1.741	1.729	1.746	–	–
$3p \to 3d$	1.547	1.552	1.555	1.544	1.741
$3d \to 3s$+abs.	0.186	0.187	0.185	0.182	0.207
$3d \to 3p$	0.928	0.931	0.933	0.927	1.044
$3d \to 3d$	1.012	0.998	0.998	–	–

Table 1 shows cross–sections for $(\pi^- p)_{n=3}$ scattering from hydrogen atoms at the kinetic energy 73 eV. The models discussed above except the FF approximation are in good agreement with each other. Absorption can take place either during the collisions or after Stark transitions to the $3s$ state. The distinction is, however, artificial as it depends on how large one defines the collision zone and it is not important in the present context ($n = 2{-}4$, 10 bar) because the ns states are so short–lived that they are almost completely depleted between the collisions.

Figure 2 shows the energy dependence for the l–averaged Stark cross–sections

$$\sigma_n^{\mathrm{Stark}} = n^{-2}\sum_{l=0}^{n-1}(2l+1)\sum_{l'\neq l}\sigma_{nl\to nl'}. \quad (23)$$

The FF approximation overestimates the cross–sections by up to 33% (at $n = 2$ and 220 eV). It generally becomes better as the kinetic energy decreases: for example, for the Coulomb component at $n = 3$ with the kinetic energy 73 eV the Stark cross–section in the FF approximation is 13% above the SLT one. In order to understand the origin of this effect we calculated the contributions to the $2p \to 2s$ cross–section from different impact parameters at the kinetic energies 209 eV and 1 eV (Figs. 3 and 4). The latter was chosen only for clarification purposes: the $2s$ shift and widths are very important at low energies. The range of impact parameters which contribute to the cross–sections can be divided into two parts: small impact parameters where the phases are saturated and large impact parameters where perturbation theory applies.

[1] The $2p - 2s$ energy difference is largely given by strong interaction (0.89 eV [4]), first order vacuum polarization (0.33 eV), and relativity (0.03 eV). Small contributions like finite size effects and higher order QED corrections are not included in the calculations.

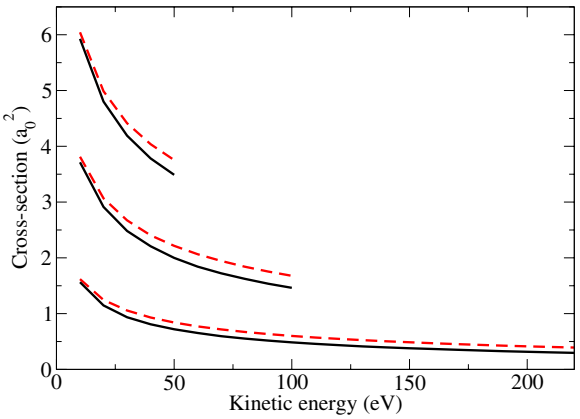

Fig. 2. The energy dependence of the Stark cross–sections for $\pi^- p$ with the principal quantum number $n = 2-4$ scattering from hydrogen atoms. The result of the SLT approximation is shown with solid lines, that of the FF approximation with dashed lines.

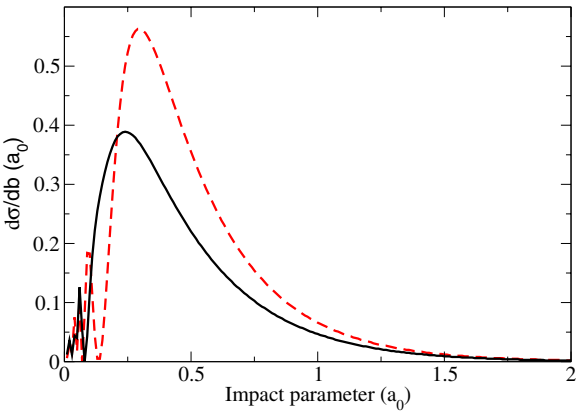

Fig. 3. The contributions to the cross–section $2p \rightarrow 2s$ at 209 eV as a function of the impact parameter. The result of the SLT model (solid lines) is shown in comparison with that of the fixed field approximation (dashed lines). The energy shift and width of the $2s$ state were set to zero.

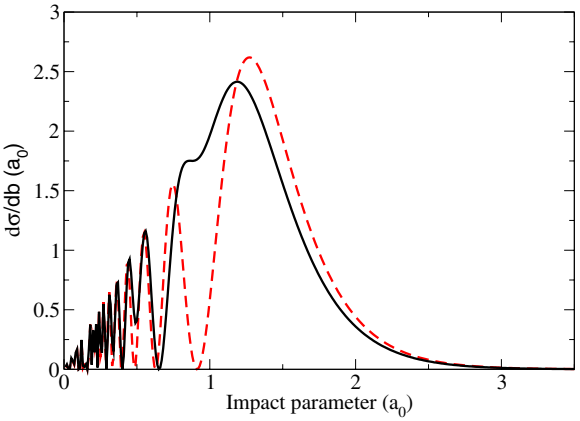

Fig. 4. The contributions to the cross–section $2p \rightarrow 2s$ at 1 eV as a function of the impact parameter. The lines are as in Figure 3.

The share of the cross–sections coming from the perturbative range increases with increasing kinetic energies.

To see why the FF approximation overestimates the cross–sections in the perturbative range one can compare the two expressions (18) and (22). As we are interested in the cross–sections that are summed and averaged over the magnetic quantum number m, we can without loss of generality consider a trajectory parallel to the z–axis in the xz–plane. The electric field component E_y is zero and the contribution to the phases from E_x will tend to cancel as this component changes sign during the passage. The important contribution in the perturbative range to the phases is, therefore, a term proportional to

$$\int_{-\infty}^{\infty} E_z(R(t))\mathrm{d}t. \tag{24}$$

This term is smaller than the corresponding one in the FF approximation

$$\int_{-\infty}^{\infty} |\mathbf{E}(R(t))|\mathrm{d}t \tag{25}$$

which explains why this approximation overestimates the cross–sections.

5.2 Scattering from hydrogen molecules

In the following, $\mathbf{R}_A$ and $\mathbf{R}_B$ denote the vectors from each of the protons in the target hydrogen molecule to the centre–of–mass of the $\pi^- p$.

The collisional rates in the case of molecular target differ from those of atomic target due to coherence effects, electric field cancellation, the geometrical size of the H_2 being smaller than two hydrogen atoms, and an electronic charge distribution that is not simply a superposition of hydrogen atom distributions. The coherence effects are most pronounced in collisions where the $\pi^- p$ trajectory is parallel to the inter–nuclear axis. For impact parameters in the range where perturbation theory is valid, constructive interference can double the atomic scattering amplitudes, thus giving a factor of four in the ratio molecular to atomic cross–sections. While the coherence effects can enhance the molecular cross–sections above twice the atomic ones, the partial cancellation of the electric fields from the two hydrogen atoms in the molecule works in the other direction.

In order to examine the sensitivity of the cross–sections to the electronic charge density three different distributions were applied. First, we used the sum of atomic $1s$ charge distributions placed around each proton corresponding to the electron density

$$\rho_I(\mathbf{R}) = (1+1/R_A)\exp(-2R_A)+(1+1/R_B)\exp(-2R_B). \tag{26}$$

where $R_A = |\mathbf{R}_A|$ and $R_B = |\mathbf{R}_B|$. The electric field in this case is a superposition of those of two hydrogen atoms:

$$\mathbf{E}(\mathbf{R}) = \frac{\mathbf{R}_A}{R_A}F(R_A) + \frac{\mathbf{R}_B}{R_B}F(R_B). \tag{27}$$

The second and third charge distributions are derived from two–center molecular orbitals. First we use the unnormalized wave function

$$\phi_{II}(\mathbf{R}) = \exp(-\lambda R_A) + \exp(-\lambda R_B) \tag{28}$$

where the variational parameter $\lambda = 1.1895$ minimizes the energy of the H_2 ground state at the inter–nuclear separation of $1.4a_0$ [26]. The electron density is given by

$$\rho_{II}(\mathbf{R}) = \frac{2|\phi_{II}(\mathbf{R})|^2}{\int |\phi_{II}(\mathbf{R}')|^2 \mathrm{d}^3\mathbf{R}'}. \tag{29}$$

A more refined result was obtained by using the Slater orbitals [27]

$$\begin{aligned}
\chi_{1s}(\mathbf{R}) &= 2\zeta_1^{3/2} e^{-\zeta_1 R} Y_{00} \\
\chi_{2s}(\mathbf{R}) &= \frac{2}{\sqrt{3}} \zeta_2^{5/2} R e^{-\zeta_2 R} Y_{00} \\
\chi_{2p_0}(\mathbf{R}) &= \frac{2}{\sqrt{3}} \zeta_3^{5/2} R e^{-\zeta_3 R} Y_{10}(\cos\theta)
\end{aligned} \tag{30}$$

where θ is the angle relative to the inter–nuclear axis. The molecular wave function is given by

$$\phi_{III}(\mathbf{R}) = a_{1s}\phi_{1s}(\mathbf{R}) + a_{2s}\phi_{2s}(\mathbf{R}) + a_{2p_0}\phi_{2p_0}(\mathbf{R}) \tag{31}$$

where

$$\begin{aligned}
\phi_{1s}(\mathbf{R}) &= \chi_{1s}(\mathbf{R}_A) + \chi_{1s}(\mathbf{R}_B) \\
\phi_{2s}(\mathbf{R}) &= \chi_{2s}(\mathbf{R}_A) + \chi_{2s}(\mathbf{R}_B) \\
\phi_{2p_0}(\mathbf{R}) &= \chi_{2p_0}(\mathbf{R}_A) - \chi_{2p_0}(\mathbf{R}_B).
\end{aligned} \tag{32}$$

The variational calculation reported in reference [27] gave $a_{1s} = 0.43262$, $a_{2s} = 0.12384$, $a_{2p_0} = 0.02827$, $\zeta_1 = 1.378$, $\zeta_2 = 1.176$, and $\zeta_3 = 1.820$. With this set of parameters the wave function is normalized to 1 so the electron density is given by

$$\rho_{III}(\mathbf{R}) = 2|\phi_{III}(\mathbf{R})|^2 \,. \tag{33}$$

The total molecular energy in this case corresponds to 96.51% of the observed value.

Two–dimensional tables for the electric field corresponding to the densities $\rho_{II}(\mathbf{R})$ and $\rho_{III}(\mathbf{R})$ were calculated in order to speed up the execution time for the numerical solution of the differential equations. We chose 500 values for the impact parameter b (measured from the center of the H_2 molecule) in steps of $0.01a_0$. For each value of the impact parameter a set of random orientations of the hydrogen molecule was selected and the matrix A was calculated as described in Section 5.1. The contribution to the cross–section from the impact parameter is then given by the average from the different molecular orientations. We chose 200, 50, and 20 orientations of the H_2 molecule for $n = 2$, 3, and 4, respectively. The statistical errors in the total cross–sections are less than 2%.

Figure 5 shows the result for the ratios $\sigma_n^{\mathrm{mol}}/2\sigma_n^{\mathrm{atom}}$ which are used by the cascade program described in Section 3. The molecular effect is smallest when the atomic charge distribution (26) is used resulting in a ratio

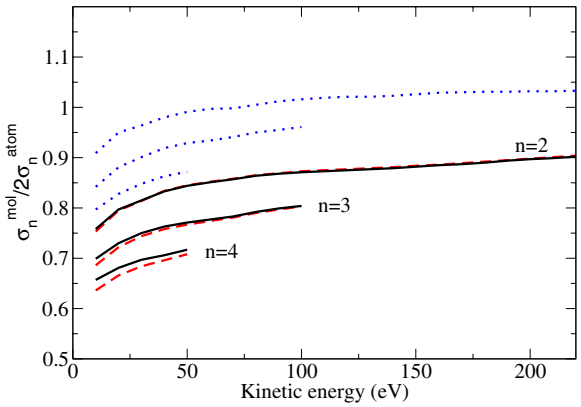

Fig. 5. The energy dependence of the ratio $\sigma_n^{\mathrm{mol}}/2\sigma_n^{\mathrm{atom}}$ for $\pi^- p$ with the principal quantum number $n = 2$–4 scattering from hydrogen. The results are shown for the electron densities ρ_I (dotted lines), ρ_{II} (dashed lines), and ρ_{III} (solid lines).

$\sigma_n^{\mathrm{mol}}/2\sigma_n^{\mathrm{atom}} = 0.8$–$1.05$ in the examined energy range. The geometric effect of molecular scattering leading to a reduction of the ratio becomes more pronounced with increasing n. This is not unexpected since the cross–sections increase with n and become comparable to the geometric size of the H_2. The use of the two more accurate charge distributions (29) and (33) reduces the ratio significantly ($\sigma_n^{\mathrm{mol}}/2\sigma_n^{\mathrm{atom}} = 0.65$–$0.9$). Since the results obtained with one and three Slater orbitals are in good agreement with each other we expect the convergence to be good.

6 Results

The cross–sections used by the cascade model for atomic hydrogen target were calculated in the SC model while the molecular corrections were obtained in the SLT approximation. The results of the cascade calculations presented here are calculated with the strong interaction width

$$\Gamma_{1s}^{\mathrm{had}} = 0.8 \text{ eV} \tag{34}$$

but the dependence on $\Gamma_{1s}^{\mathrm{had}}$ is very weak at $n = 2$–4. This is because the absorption takes place after a Stark transition to the ns state which, for a realistic range of $\Gamma_{1s}^{\mathrm{had}}$ values, decay almost completely before the next collision. As the cross–sections for the $nl \to ns$ transitions are nearly independent of the width at high energies the cascade at low n ends up being only weakly dependent on $\Gamma_{1s}^{\mathrm{had}}$. The initial state is assumed to be statistically distributed over the the angular quantum number l.

Figure 6 shows the kinetic energy distribution at the pressure 10 bar at the instant of the $3p \to 1s$ transition originating from the 34 eV component at $n = 4$. The result is calculated for molecular target with the charge distribution $\rho_{III}(\mathbf{R})$. Only $g_{34} = 3\%$ of the initial component goes through this transition with high kinetic energies — most atoms experience nuclear absorption. The figure shows that it is sensible to separate the kinetic energy distribution in high and low energy components because those

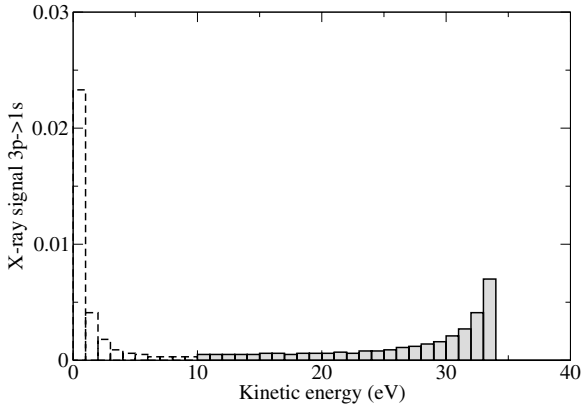

Fig. 6. The kinetic energy distribution at 10 bar at the instant of the $3p \rightarrow 1s$ transition originating from the 34 eV component at $n = 4$. The cascade simulation is based on 10^7 $\pi^- p$ atoms. The calculation does not take molecular formation and Coulomb deexcitation into account so the predicted low energy part shown with dashed bars is not reliable.

Table 2. The calculated results for g_{mn} at 10 bar using both atomic and molecular target with three different charge distributions. Each cascade simulation is based on 10^7 events.

Quantity	H	H_2 (ρ_I)	H_2 (ρ_{II})	H_2 (ρ_{III})
g_{22}	0.540	0.535	0.556	0.556
g_{23}	0.087	0.090	0.107	0.107
g_{33}	0.138	0.144	0.163	0.163
g_{24}	0.0291	0.0345	0.0448	0.0439
g_{34}	0.0188	0.0241	0.0309	0.0301
g_{44}	0.0364	0.0412	0.0484	0.0478
g_{23}/g_{33}	0.627	0.626	0.659	0.659
g_{24}/g_{34}	1.548	1.432	1.450	1.459
g_{34}/g_{44}	0.517	0.585	0.638	0.630

atoms which loose a significant fraction of their initial energy are likely to loose almost all. The reason for that is that deceleration becomes more efficient as the energy decreases due to the differential cross–sections becoming less forward–peaked.

The results for the components g_{mn} are given in Table 2 for the pressure 10 bar. Taking molecular target effects into account by using the most accurate charge distribution, $\rho_{III}(\mathbf{R})$, increases all components, g_{mn}, compared to the atomic case. This is a consequence of the Stark rates being smaller for molecular target: the ns states from which nuclear absorption takes place are populated less efficiently in this case so more $\pi^- p$ atoms survive and go through the radiative transitions.

Some of the components are very sensitive to the molecular effects: g_{24} and g_{34} are increased by 51% and 60%, respectively. However, only the ratios are needed in the analysis described in Section 4. The largest molecular effect (22%) is found for g_{34}/g_{44}.

The main purpose of the present investigations is to provide the framework for the determination of the $1s$ strong interaction width from the K X–ray spectra. The fitting procedure described in Section 4 has not been carried out yet so we do not know how sensitive the resulting value for $\Gamma_{1s}^{\rm had}$ will be to, for example, uncertainties in the cross–sections and the arbitrary choice of 10 eV as separating high and low energies. The assumption that the highly $\pi^- p$ atoms are produced with the characteristic energies given by equation (6) also needs some modification if Coulomb deexcitation via molecular states is important: because the states $\{\pi^- pp\}^*$ lie below the $(\pi^- p)_n + p$ dissociation limit there will be less kinetic energy available after a Coulomb transition. These issues will be the subject of careful studies in the future.

6.1 Estimating the Coulomb deexcitation rates

The results obtained by analyzing the X–ray spectra can be used to improve our understanding of the cascade processes. An example of an interesting quantity is (using Eq. (14))

$$\frac{Y_{n-1}^{\rm Coul}}{Y_n^{\rm rad} f_n^{\rm low}} = \frac{Y_{n-1}^{\rm rad}}{Y_n^{\rm rad}} \frac{f_{n-1n-1}}{f_n^{\rm low}} \frac{1}{g_{n-1n-1}} \qquad (35)$$

which can be calculated once the fitting procedure has yielded the weights $f_n^{\rm low}$ and f_{n-1n-1}. Equation (35) is the ratio between the Coulomb and the radiative deexcitation rates for the low energy component at the level n. It is theoretically interesting because it can be predicted without considering the whole atomic cascade but only the case of low energy $\pi^- p$ atoms with quantum number n scattering from H_2 molecules. By comparing predicted and measured results for the ratio (35) different models (for example those including molecular formation) for calculating the collisional processes can be tested.

7 Conclusion

A method for extracting the $1s$ strong interaction width of pionic hydrogen from K X–ray spectra has been discussed. The proposed method combines a fitting procedure for the weights of the high energy components with cascade model constraints in different $np \rightarrow 1s$ spectra. The constraints are results of cascade calculations for $\pi^- p$ in hydrogen gas for the high energy components taking into account nuclear absorption, deceleration, and Stark, Auger, and radiative transitions. In addition to the cascade calculations, the X–ray intensity ratios $K_\alpha/K_\beta/K_\gamma$ are needed.

Various frameworks were used to calculate the cross–sections for the collisional processes. In the relevant energy region (>10 eV), the semiclassical straight–line trajectory approximation was found to be in good agreement with the more accurate close coupling model. The often used fixed field approximation, where the electric field from the target atom is assumed to be directed along the z–axis during the collision, is a fair approximation: it overestimates the cross–sections by up to 33% for the highest energies.

After the proposed method has been applied successfully in determining the weights of the high energy components, it is possible to obtain the Coulomb deexcitation

rates for the low energy components. This could stimulate new theoretical studies of the Coulomb deexcitation process for example regarding the role of molecular formation.

The author would like to thank L. Simons and D. Gotta for many fruitful and stimulating discussions. This work was supported by the Swiss National Science Foundation.

References

1. D. Gotta, Prog. Part. Nucl. Phys. **52**, 133 (2004)
2. S. Deser et al., Phys. Rev. **96**, 774 (1954)
3. J. Gasser et al., Eur. Phys. J. C **26**, 13 (2002)
4. H.C. Schröder et al., Eur. Phys. J. C **21**, 473 (2001)
5. D.F. Anagnostopoulos et al., Nucl. Phys. A **721**, 849c (2003)
6. M. Leon, H.A. Bethe, Phys. Rev. **127**, 636 (1962)
7. E. Borie, M. Leon, Phys. Rev. A **21**, 1460 (1980)
8. T.P. Terada, R.S. Hayano, Phys. Rev. C **55**, 73 (1997)
9. V.E. Markushin, Phys. Rev. A **50**, 1137 (1994)
10. T.S. Jensen, V.E. Markushin, Eur. Phys. J. D **19**, 165 (2002)
11. T.S. Jensen, V.E. Markushin, Eur. Phys. J. D **21**, 261 (2002)
12. T.S. Jensen, V.E. Markushin, Eur. Phys. J. D **21**, 271 (2002)
13. T.S. Jensen, V.E. Markushin, in *Precision Physics of Simple Atomic Systems*, edited by S.G. Karshenboim, V.B. Smirnov, Lecture Notes in Physics **627** (Springer, Berlin, 2003), p. 37
14. J.S. Cohen, Phys. Rev. A **59**, 1160 (1999)
15. L. Bracci, G. Fiorentini, Nuovo Cim. A **43**, 9 (1978)
16. L.I. Ponomarev, E.A. Solov'ev, Hyperf. Interact. **119**, 55 (1999)
17. S. Jonsell, J. Wallenius, P. Froelich, Phys. Rev. A **59**, 3440 (1999)
18. A. Badertscher et al., Europhys. Lett. **54**, 313 (2001)
19. R. Pohl et al., Hyperf. Interact. **138**, 35 (2001)
20. R. Pohl et al., in *Precision Physics of Simple Atomic Systems*, edited by S.G. Karshenboim et al., Lecture Notes in Physics **570** (Springer, Berlin, 2001), p. 454
21. A.J. Rusi El Hassani et al., Z. Phys. A **351**, 113 (1995)
22. G. Kodosky, M. Leon, Nuovo Cim. B **1**, 1 (1971)
23. J.S. Cohen, M.C. Struensee, Phys. Rev. A **38**, 53 (1988)
24. K. Sakamoto, J. Phys. B: At. Mol. Opt. Phys. **35**, 997 (2002)
25. G. Reifenröther, E. Klempt, Phys. Lett. B **248**, 250 (1990)
26. J.C. Leclerc, J. Phys. B: At. Mol. Phys. **7**, L281 (1974)
27. S. Fraga, B.J. Ransil, J. Chem. Phys. **35**, 1967 (1961)